

A Plasma Torus Around a Young Low-Mass Star

Luke G. Bouma^{1,2}

¹*Observatories of the Carnegie Institution for Science, Pasadena, CA 91101, USA*

²*Department of Astronomy, California Institute of Technology, Pasadena, CA 91125, USA*

³*Carnegie Fellow; 51 Pegasi b Fellow*

Roughly one percent of red dwarfs younger than 100 million years show structured, periodic optical light curves suggestive of transiting opaque material that corotates with the star^{1–4}. The composition, origin, and even the existence of this material are uncertain. The main alternative hypothesis is that these complex periodic variables (CPVs) are explained by complex distributions of bright or dark regions on the stellar surfaces⁵. Here, we present time-series spectroscopy and photometry of a rapidly-rotating ($P=3.9$ hr) CPV, TIC 141146667. The spectra show coherent sinusoidal Balmer emission at twice to four times the star’s equatorial velocity, directly demonstrating for the first time the existence of corotating circumstellar plasma around a CPV. Given that long-lived condensations of cool (10^4 K) plasma can persist in the hot (10^6 K) coronae of stars with a wide range of masses^{6–11}, these data support the idea that around the lowest-mass stars, such condensations can sustain an optically thick component; the origin of the optically thick material and its microphysical opacity remain unclear.

1 Main

M dwarfs, stars with masses below about half that of the Sun, are the only type of star to offer near-term prospects for detecting the atmospheres of rocky exoplanets with surface water¹². Community investment with JWST has proceeded accordingly^{13,14}. How an M dwarf’s evolution influences its planets—especially the retention of their atmospheres—has in turn become a major theme in exoplanet and stellar astrophysics. Previous work has established that most M dwarfs host close-in planets¹⁵ that on average are subject to long circumstellar disk lifetimes¹⁶, to large doses of UV radiation¹⁷, and to a high incidence of flares and coronal mass ejections¹⁸. However, despite extensive work in these areas, the plasma and magnetospheric environments that bathe young, close-in exoplanets remain challenging to quantify. Understanding these environments is crucial because they directly impact atmospheric retention and habitability of close-in planets.

One glaring example of our current ignorance is the complex periodic variables (CPVs). While Figure 1 highlights the main object of interest in this article, over one hundred analogous objects have now been found by K2 and TESS^{1–4,19,20}. These CPVs are phenomenologically identified based on their structured, periodic optical light curves; most are M dwarfs with rotation periods shorter than two days. Within current sensitivity limits, none have primordial disks^{2,4}. However, $\approx 3\%$ of stars a few million years old show this behavior, an observed fraction which decreases to $\approx 0.3\%$ by ≈ 150 Myr²⁰.

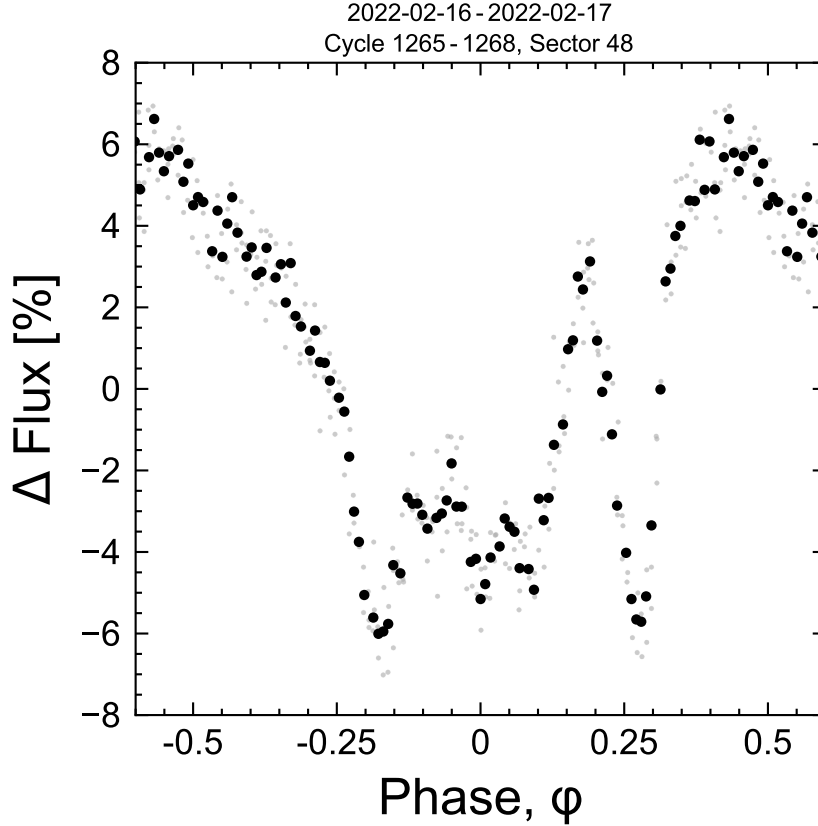


Figure 1 (Movie): TIC 141146667 is a complex periodic variable (CPV). The online movie, available [here](#), covers a baseline of 5,784 cycles irregularly sampled over three years. The TESS light curve is phased to the 3.930 hour period in groups of a few cycles per frame. This is the period both of stellar rotation, and (we hypothesize) of corotating clumps of circumstellar material. Raw data acquired with two minute sampling are in gray; black averages to 100 points per cycle. Similar to other stars of this class, the sharp photometric features persist for tens to thousands of rotational cycles.

The two leading hypotheses to explain the CPVs are either that transiting clumps of circumstellar material corotate with the star ^{2,4,21}, or that these stars represent an extreme in naturally-occurring distributions of starspots or faculae ⁵. The main argument against a starspot-only explanation invokes the timescales and amplitudes of the sharpest photometric features. However, no independent evidence has yet been acquired for the presence of any circumstellar material. Geometrically, transiting clumps would imply an occurrence a few to at most ten times the observed rate. The clumps could therefore exist around 10-30% of M dwarfs during their early lives.

The dearth of evidence for circumstellar material around CPVs is surprising given that separate studies of young stars have, for decades, reported that stellar coronae contain both hot (10^6

K) and cool (10^4 K) plasma. In particular, time-series spectra of stars with a wide range of masses have shown periodic high-velocity absorption and emission in Balmer lines such as $H\alpha$, interpreted as long-lived, corotating clumps of cool plasma^{6,8,22–27}. Such clumps are thought to be forced into corotation by the magnetic field, and the exact geometry of where the plasma can accumulate is dictated by the field’s topology. For instance, a tilted dipole field tends to yield an accumulation surface of a warped torus⁷, whereas in the limit of a single strong field line, accumulation occurs at the line’s apex, furthest from the star¹⁰. To date, none of these spectroscopic variables have shown any photometric anomalies⁴, leaving open the issue of whether they are related to CPVs.

In this study, we present the first spectroscopic detection of corotating clumps of cool plasma around a CPV. We identified TIC 141146667 in previous work⁴ by searching the TESS two-minute data²⁸ for stars showing highly structured, periodic light curves. We selected the star for spectroscopy because its brightness and rotation rate enable measuring variability in its line profile. We observed it for five hours on 17 February 2024 (UT) using the High Resolution Echelle Spectrometer (HIRES²⁹) on the 10 m Keck I telescope. TESS observed the star over a four week interval from 30 January 2024 to 26 February 2024 with a duty cycle of 77%. During the HIRES observations, TESS was performing a data downlink; TESS data collection resumed 12 hours (three rotation cycles) after the spectra were acquired. Extended Data Figure 1 shows the detailed photometric behavior of the star near the epoch of observation; the general photometric morphology is similar before and after the data gap.

2 Results

Figure 2 compiles the TESS and HIRES data from February 2024. Over timescales of years, CPVs maintain a fixed period while their photometric morphology evolves. TIC 141146667 indeed evolved relative to the February 2022 discovery data (see Figure 1). In February 2024, the average photometric signal showed a small brightening over 45% of the period, followed by a complex flux dip spanning 55% of the period. This eclipse feature shows two to three local photometric minima, and one to two local maxima. Its W-shape is suggestive of eclipse geometries seen in forward models of warped plasma tori (see³⁰ and the associated movies).

The spectroscopy shows emission beyond the star’s equatorial velocity ($v_{\text{eq}}=130 \text{ km s}^{-1}$). There are at least two distinct emission components, separated by half a cycle in phase. The first component has clearer sinusoidal behaviour and is double-peaked, with peak semi-amplitudes of $K_1=2.1 v_{\text{eq}}$ and $2.7 v_{\text{eq}}$. There is significant non-periodic variability in the emissivity of this double-peaked component: the flux excess begins with an amplitude of 70% above the continuum early in the observation sequence, and diminishes to 10% by its end. The component 180° opposite in phase is detected only from $\phi=0.2$ -1.0. From $\phi=0.2$ -0.5, this latter component appears connected to the star in velocity space. While its peak semi-amplitude of $K_1=3.9 v_{\text{eq}}$ is achieved at both $\phi=0.25$ and 0.75 , its amplitude similarly decreases from a 60% excess over the continuum at the beginning of the observation sequence to a 10% excess by its end. The apparent period for all of

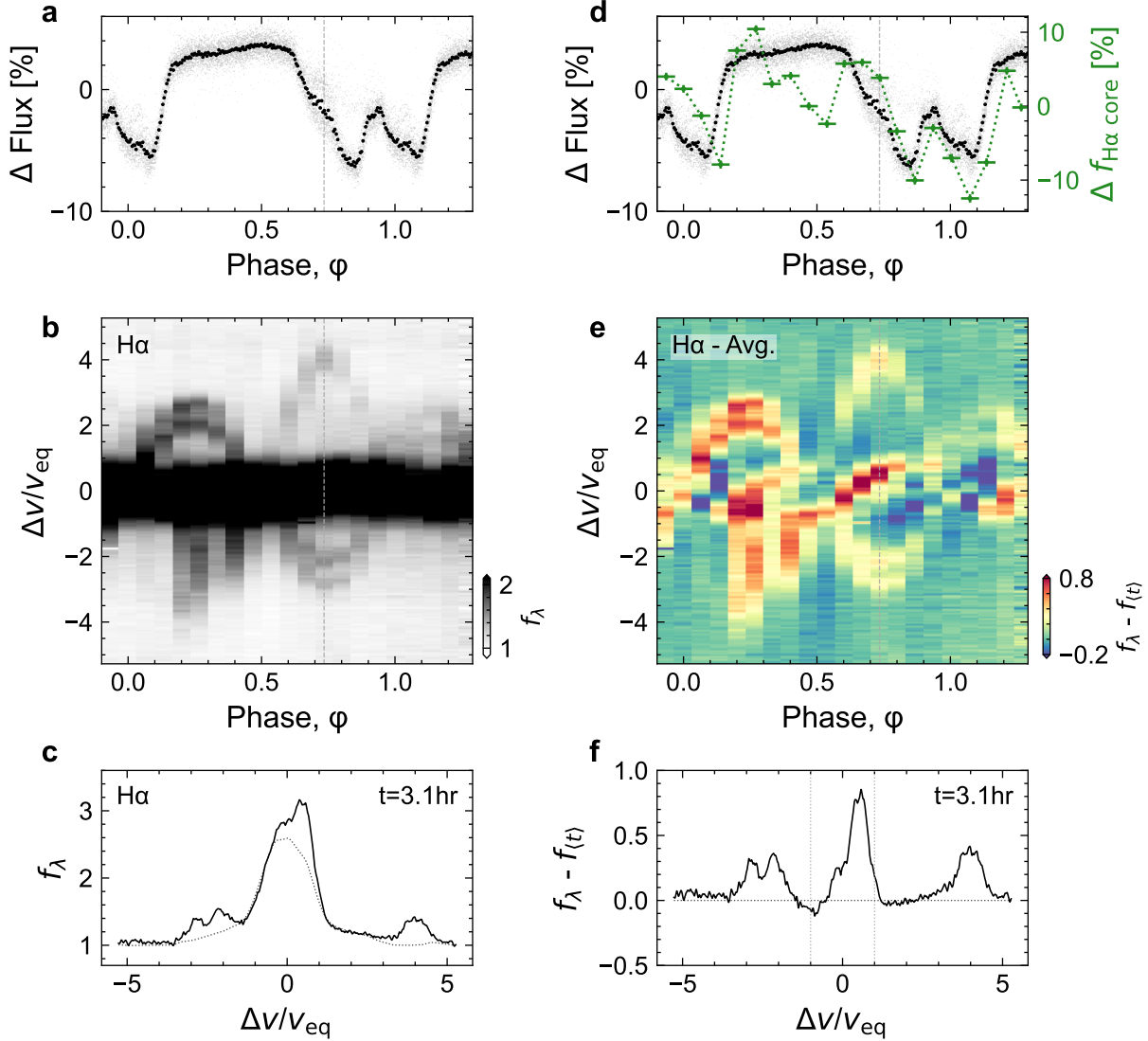


Figure 2 (Movie): Emission from circumstellar plasma orbiting TIC 141146667. The online movie, available [here](#), shows the spectral evolution over five hours. **a**, Average TESS light curve from 5 February 2024 to 26 February 2024 folded on the 3.930 hour period. Black points are phase-averaged; gray are the raw data. **b**, Keck/HIRES H α spectra acquired on 17 February 2024. The continuum is set to unity, and the darkest color is at twice the continuum to accentuate emission outside the line core ($|v/v_{\text{eq}}| > 1$, for $v_{\text{eq}}=130 \text{ km s}^{-1}$). While emission in the line core originates in the star’s chromosphere, the sinusoidal emission features are most readily described by a warped plasma torus. **c**, Individual epochs of Panel b, visible in the online movie. The dotted line shows the time-averaged spectrum, $f_{(t)}$. **d**, As in Panel a, but overplotting the median-normalized H α light curve at $|v/v_{\text{eq}}| < 1$. **e**, As in Panel b, after subtracting the time-averaged spectrum. The line core shows H α excesses and decrements advancing from the blue to red wings. The asymmetric color stretch is set to mirror the dynamic range of the data. **f**, Individual epochs of Panel e, visible in the online movie.

these emission components is consistent with the photometric 3.930 hour period.

These sinusoidal emission features require circumstellar clumps of partially-ionized hydrogen to corotate with the star. Based on the period, this material's motion is not Keplerian; it can only be explained by plasma being dragged along with the rotating stellar magnetic field. The velocity semi-amplitude of the sinusoids gives the distance of the clumps from the stellar surface: 2.1-2.7 R_\star for the closer clump, and 3.9 R_\star for the other. These clumps transit in front of the star when passing from negative to positive velocity. This implies that the spectroscopic transit of the 2.1-2.7 R_\star clump occurs simultaneously with the sharp photometric spike visible in the TESS data.

The data in the $H\alpha$ line core are more complex. At $|\Delta v/v_{\text{eq}}| < 1$, most observed $H\alpha$ photons come from the star's chromosphere; circumstellar material may additionally modulate the line profile. Figure 2e suggests line core variability caused by both bright and dark regions on the star's surface, superposed with smaller-amplitude variability from the transiting circumstellar material. For instance, from $\phi=0$ -0.3, the double-peaked emission feature is visible when it is being viewed both on and off-limb. However, the large emission feature that crosses the star from $\phi=0.4$ -0.9 cannot be circumstellar in origin; it emits at an amplitude greater than that observed from the circumstellar components, and it crosses the stellar velocity surface too slowly. It must therefore originate from a chromospherically bright region near the stellar surface. While the origin of the other bright and dark streaks passing across the line core are more ambiguous, a final exercise to quantify the behavior of this region is shown in Figure 2d, where $f_{H\alpha \text{ core}}$ denotes the summed flux at $|\Delta v/v_{\text{eq}}| < 1$. This panel shows that changes in the line core flux correlate with the broadband variability throughout most of the light curve, except near $\phi \approx 0.5$, corresponding to the transit of the 3.9 R_\star clump and the occultation of the lower-velocity clump.

3 Discussion

Spectra of magnetically-active, rapidly rotating stars with a wide range of masses have been known to exhibit both sinusoidal emission features^{7,8,24,25} and transient absorption features^{6,22,33} similar to Figure 2. No such stars were previously known to show complex light curves⁴. One interpretation for such spectroscopic variability comes from an analogy to quiescent solar prominences, which are cool condensations of plasma in the solar corona that can last days to weeks³⁴. These condensations fall back to the Sun's surface because gravity is stronger than any magnetic tension or centrifugal force capable of sustaining them. However for stars with magnetospheric radii R_m that exceed their corotation radii R_c , the effective potential experienced by a charged particle can have a local minimum outside R_c , enabling the material to accumulate over much longer timescales^{9,11}. Generally speaking, such material need neither transit, nor be optically thick. For instance, the $H\alpha$ emission clump at 3.9 R_\star shows no photometric signal in the February 2024 photometry.

Our Keck/HIRES observations are the first reported time-series spectra of a CPV, and they show that corotating circumstellar plasma clumps are present around at least one such star. This

Table 1: Selected System Parameters for TIC 141146667

Parameter	Description	Value	Source
T_{eff}	Effective Temperature (K)	2972 ± 40	1
R_{\star}	Stellar radius (R_{\odot})	0.42 ± 0.02	1
Age	Stellar age range (Myr)	35-150	2
M_{\star}	Stellar mass (M_{\odot})	0.22 ± 0.02	3
γ	Systemic radial velocity (km s^{-1})	0.61 ± 1.47	4
Spec. Type	Spectral Type	M5.5Ve	4
P_{rot}	Rotation period (hr)	3.930 ± 0.001	5
v_{eq}	Equatorial velocity ($2\pi R_{\star}/P_{\text{rot}}$) (km s^{-1})	130 ± 4	6
$v_{\text{eq}} \sin i_{\star}$.	Projected rotational velocity (km s^{-1})	138 ± 8	4
v_{break}	Breakup velocity ($GM_{\star}/R_{\star})^{1/2}$ (km s^{-1})	316 ± 16	6
i_{\star}	Stellar inclination 2σ lower limit (deg)	>63	4
d	Distance (pc)	57.54 ± 0.09	7
R_{c}	Keplerian corotation radius (R_{\star})	1.82 ± 0.10	6
a_1	Clump 1 orbital radius (R_{\star}) . . .	2.1-2.7	4
a_2	Clump 2 orbital radius (R_{\star}) . . .	3.9	4
$\langle \text{EW}_{\text{H}\alpha} \rangle$	Time-averaged H α line core equivalent width (\AA)	7.2 ± 0.2	4

NOTE— Provenances are: 1: SED fit ⁴. 2: Gaia DR3 photometry shows the star is on the pre-main sequence, while the spectrum lacks lithium (see 3). 3: PARSEC v1.2S ³¹. 4: Keck/HIRES. 5: TESS light curve. 6: Derived quantity. 7: Gaia DR3 geometric ³².

observation rules out a “starspot-only” origin for the CPVs,⁵ because such scenarios have no means of explaining spectroscopic emission beyond the stellar disk. Similarly, scenarios in which the circumstellar material is made only of dust are also ruled out. While dust may be present, to explain the H α emission the clumps must include plasma with a significant population of hydrogen atoms in the $n=3$ excited state, where n denotes the principal quantum number. More quantitatively, the observed H α luminosity suggests characteristic densities and masses for the gaseous component of these clumps of $n_{\text{H}} \sim 10^{11}\text{-}10^{12}\text{ cm}^{-3}$ and $M_{\text{gas}} \sim 10^{17}\text{ g}$ (see Section 3). Dust, if present, is independently constrained to have a total mass $10^{15}\text{ g} < M_{\text{dust}} < 10^{17}\text{ g}$ (see Section 3). This circumstellar material could originate either from the star or from an external source. Plausible external sources include an old and undetected disk, comets, or a close-in exoplanet. This latter scenario would make CPVs extrasolar analogs of the Jupiter-Io plasma torus (e.g. Ref.³⁵).

The other potential analog for the CPVs are the σ Ori E variables, a rare subset of B stars with radiatively-driven winds that accumulate into warped plasma tori^{7,30}. These tori tend to have dense antipodal accumulations of plasma sculpted by tilted-dipole magnetic fields, and the transits of these clumps produce broadband photometric variability through bound-free scattering⁷ and Thomson scattering³⁶. The plasma accumulates at antipodes 180° apart because the deepest local minima in the effective potential exist along the line of intersection between the rotational and magnetic equators (see Equation 22 of⁷). For σ Ori E and almost all of its analogs, the result is light curves that appear “simple”, resembling those of eclipsing binaries, and time-dynamic H α spectra similar to those in Figure 2^{7,30}. The two known exceptions, HD 37776 and HD 64740, show complex light curves resembling CPVs^{4,37} and have spectropolarimetric magnetic field maps indicating strong contributions from higher-order magnetic moments^{38,39}. There are two implications: first, the complexity of CPVs may be a direct consequence of magnetic fields with highly multipolar contributions. Second, CPVs can be a source of astrophysical false positives in photometric classification of eclipsing binaries and transiting exoplanets around young pre-main sequence M dwarfs^{40,41}.

Pressing issues for future work include determining the composition and origin of the circumstellar material, understanding the exact role of the stellar magnetic field, and exploring the implied space weather experienced by the close-in rocky exoplanets that, statistically¹⁵, are likely to be present in most CPV systems.

The material’s composition – either pure plasma, or else a dusty plasma – can be clarified by time-series optical and infrared spectrophotometry. While observations of CPVs in the optical suggest a chromaticity consistent with dust^{21,42,43}, a gray opacity source such as electron scattering in a plasma transiting over starspots might also produce chromatic features⁴⁴. The composition and size distribution of any dust that is present could be determined by measuring the extinction curve for one or more CPVs from 1-20 μm . Composition and size distributions similar to debris from rocky bodies seen around white dwarfs⁴⁵ would indicate a rocky-body origin. Compositions and sizes similar to the interstellar medium could be indicative of condensed dust in an M dwarf wind, similar to that formed in the environments of more evolved stars⁴⁶.

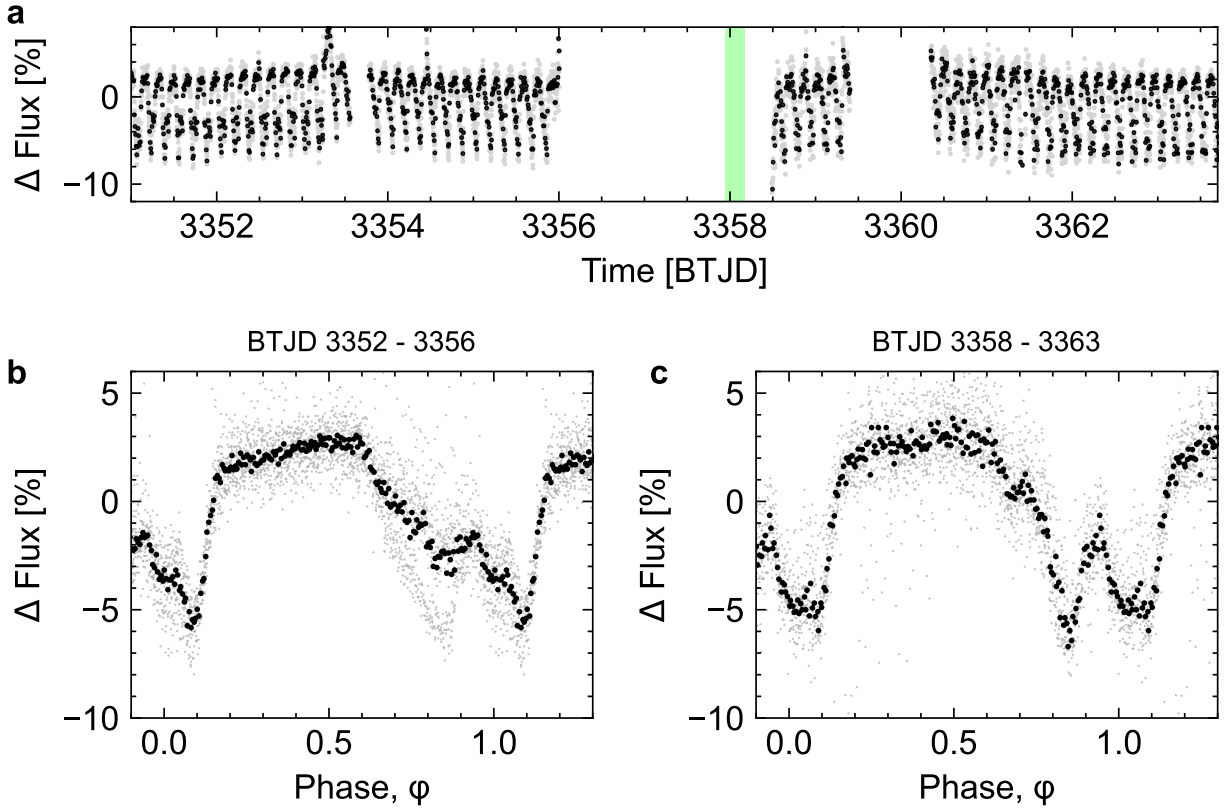
The role of the star’s magnetic field could be better understood through new observations, and new theory. From the theoretical perspective, there is an urgent need for rigid-field magnetohydrodynamic modeling to go beyond previous work^{7,30,47} and to explore what field topologies might explain the observed light curve morphologies⁴. In particular, dynamo simulations of fully-convective M dwarfs have suggested that global-scale mean fields might be confined to a single hemisphere⁴⁸; such fields would yield accumulation surfaces quite different from those that have previously been explored. Observationally, spectropolarimetry has the potential to assess both the field strength and topology. An independent constraint on magnetic field topology may also come from radio observations, which have shown⁴⁹ that CPVs emit variable radio signals, including persistent and polarized components. Detecting radio emission produced by an electron cyclotron maser instability (e.g.⁵⁰) in particular would provide a measurement of the field strength at the site of the emitting region, further clarifying the magnetosphere’s structure.

It is currently unclear what, if any, relationship CPVs have to the close-in rocky exoplanets that exist around most M dwarfs¹⁵. However, 0.3-3% of young M dwarfs show the CPV phenomenon²⁰, and our data show that the complex photometric features occur when clumps of circumstellar material transit the star. The implied geometric correction suggests that an appreciable minority (10-30%) of young M dwarfs – the rapidly rotating ones with centrifugal magnetospheres – host similar circumstellar environments to the CPVs. Future studies that combine spectroscopic, polarimetric, and multi-wavelength observations, along with magnetohydrodynamic modeling, will be key to understanding the complex magnetospheric environments of these young stars.

Methods

Observations & Data Reduction

Photometry: TESS observed TIC 141146667 ($T=13.3$) in Sectors 14, 15, 21, 41, 48, and 75. Two-minute data were acquired during Sectors 41, 48 (TESS DDT039, PI: Kunimoto), and 75 (TESS Program G06030, PI: Bouma). The data from Sectors 14, 15, and 21 had 30-minute cadence, which smears sharp features over the <4 hour period (see ²¹). The field is not crowded: the nearest known star, TIC 141146666 ($T=14.5$), is $25''$ from TIC 141146667 and is photometrically stable in the pixel-level TESS data.



Extended Data Figure 1: Photometric evolution of TIC 141146667 near the Keck/HIRES observation (green bar). **a**, TESS simple aperture photometry. The main data gaps were caused by scattered light from the Earth (BTJD 3356-3358.5) and Moon (BTJD 3359.5-3360.5). Raw two minute data are in gray; black time-averages to ten minute sampling. **b-c**, Folded light curve before and after spectroscopy. Raw two minute data are in gray; black phase-averages to 100 points per cycle. During BTJD 3352-3356, a state switch occurred near BTJD 3353, in which the dip at $\phi \approx 0.8$ disappeared. While the large eclipse feature was present both before and after the HIRES sequence, its photometric shape evolved during the data gap.

Figure 1 shows the TESS Sector 75 data acquired near the epoch of spectroscopy. The gap in coverage from BTJD 3356.0 - 3358.5 occurred because the Earth was within 25° of the TESS camera’s boresight, yielding high levels of scattered light; this gap included the Keck/HIRES observation epoch (green bar). From BTJD 3359.4 - 3362.0, the Moon then passed within 25° of the camera’s boresight. Based on the observed level of scattered light in the optimal TIC 141146667 aperture, we manually masked out times from 3359.40 - 3360.13, and judged the remainder of the data during the lunar approach to be usable. Small data gaps from BTJD 3353.55 - 3353.77 and from BTJD 3360.12 - 3360.33 were caused by data downlinks at the spacecraft’s perigee and apogee, respectively.

Figure 1 shows that a large, complex eclipse feature was present before and after the HIRES data were acquired. From BTJD 3352 - 3356, this eclipse had two sharp local minima; the local minimum at $\phi \approx 0.8$ disappeared following the flare at BTJD 3353, yielding an eclipse more closely resembling a long “V” than a “W”. Similar state changes have previously been noted and discussed^{2,4}. The photometric shape therefore evolved during the twelve cycles spanning the 3356 - 3358 gap, since the average shape from 3358-3363 more closely resembles the initial “W”.

Spectroscopy: We observed TIC 141146667 ($V=16.2$) with Keck/HIRES for five hours during the second half of the night, spanning 17 February 2024 10:47 to 16:13 (UT). The star’s airmass over this window spanned $z=1.2$ - 2.2 , and we opted for a fixed 15 minute cadence over the entire sequence, except for a final 10 minute exposure due to increasing sky brightness at sunrise. We observed without the iodine cell and used the C2 decker ($0''.86 \times 14''.0$) in the red instrument configuration, yielding a spectral resolution $R \approx 45,000$ ($\delta v \approx 6.7 \text{ km s}^{-1}$; $\delta v/v_{\text{eq}} \approx 0.05$). We binned the CCD readout by a factor of three in the spatial dimension, yielding $\approx 1,000$ photons (S/N=33) per pixel in the continuum at 6500 \AA , at minimum airmass. Strong winds contributed to $1''.2 \pm 0''.2$ seeing over the night, but conditions were otherwise favorable. We reduced the echelleogram to a one-dimensional spectrum using the standard techniques of the California Planet Survey⁵¹. Figure 2b shows the result in the vicinity of $H\alpha$ without any additional processing.

Stellar Parameters

Radial Velocity—We measured radial velocities of TIC 141146667 from our HIRES spectra using a pipeline that we developed for rapidly rotating stars. Our method is based on template-matching against synthetic spectra produced by the PHOENIX stellar atmosphere code⁵². We used the PHOENIX models with solar metallicity and alpha element abundances, and calibrated our pipeline using the standard stars described by⁵³. We used velocity standards spanning spectral types from G2 to M4 (Barnard’s Star), irrespective of rotation rate. We used `barycorrpy`⁵⁴ to calculate the velocity corrections due to Earth’s motion around the solar system barycenter and due to Earth’s daily rotation about its axis. Our analysis code reproduces the systemic velocities of known velocity standards⁵³ with an RMS of 0.66 km s^{-1} .

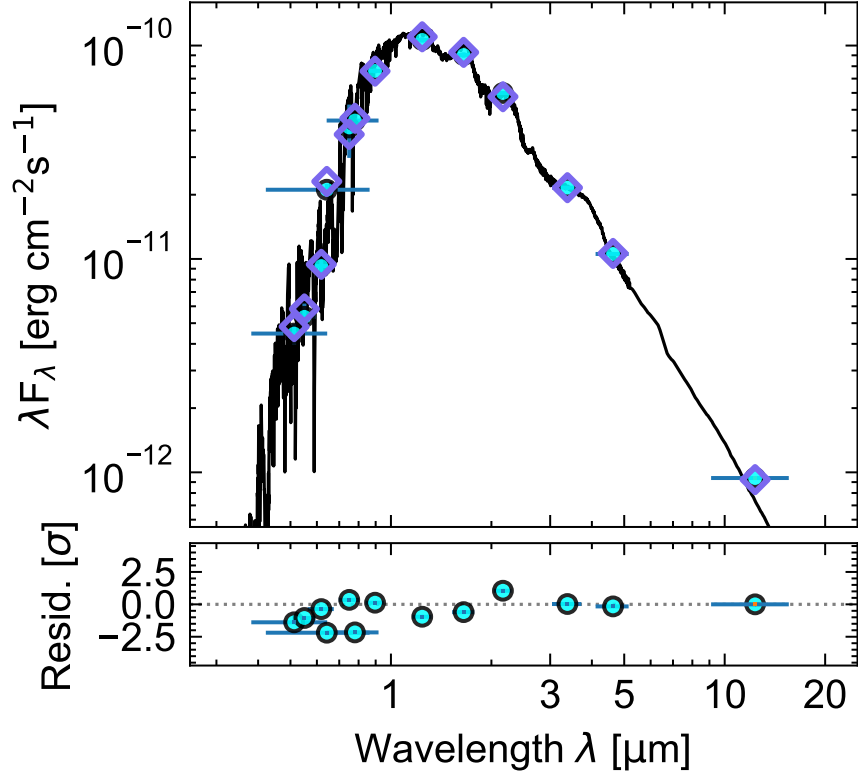
For TIC 141146667, we measured the radial velocities using regions near the K I (7700 \AA) resonance line and three TiO bandheads (5160 \AA , 5450 \AA , and 5600 \AA). We selected these regions

because they provided the best matches between the synthetic and observed spectra. We then averaged the resulting redshift measurements over each order to produce the final measurement. We used the scatter of resulting velocity measurements between orders to assign the RV uncertainty at each epoch. The uncertainty-weighted mean systemic velocity over all epochs on 17 February 2024 was $\gamma=0.6\pm1.5\text{ km s}^{-1}$. The relative radial velocities about this mean are given in Table 2.

Viewing Orientation—We fitted the rotational broadening of the K I (7700 Å) resonance line using the kernel suggested by ⁵⁵; taking the mean and standard deviation of the resulting value over all epochs yielded $v_{\text{eq}} \sin i=138\pm8\text{ km s}^{-1}$, consistent with the visual line broadening $\Delta\lambda\approx3\text{ Å}$. The star’s equatorial velocity v_{eq} based on its apparent size and rotation period is $130\pm4\text{ km s}^{-1}$. While this suggests that the viewing orientation could be nearly edge-on, the formal constraint is rather weak, with $i>63^\circ$ at 2σ (2.5th percentile of the inclination posterior).

No Evidence For Binarity—Any periodicity in the radial velocity time-series is ruled out at the rotation period for semi-amplitudes above 2.85 km s^{-1} (at 3σ confidence). This sets an upper limit on the mass of any putative companion at the four hour period of $m \sin i < 2.4 M_{\text{Jup}}$. Regarding possible companions at wider separations, the Gaia DR3 renormalized unit weight error (RUWE), a proxy for the goodness of fit for a single-source astrometric model to the Gaia astrometry, is 1.23, within the usual range for apparently single sources. There are no resolved companions in the Gaia DR3 point source catalog. Finally, we checked the TESS light curve for evidence of secondary photometric periods by subtracting the mean CPV signal over each sector and performing a phase-dispersion minimization analysis ^{56,57}. There were no secondary periods in the TESS data. Previous work ⁴ has shown that about 30% of CPVs show evidence for excess noise above the Gaia single-source astrometric model, and about 40% of CPVs show evidence for unresolved binary companions based on the presence of secondary photometric periods. This agrees with analyses showing that multi-periodic low-mass stars are generally unresolved binaries ⁵⁸. Overall, the CPV binary fraction seems consistent with that for field M dwarfs ⁵⁹, pointing to a weak or non-existent connection between the CPV phenomenon and (wide) binarity. For TIC 141146667 specifically, although we find no evidence for stellar multiplicity, our data are minimally constraining for the scenario of a low-luminosity companion ($F_1/F_2\lesssim0.1$) with apparent separation below $0''.1$.

Effective temperature, radius, mass, and spectral classification—We adopted the star’s effective temperature and radius measured using the spectral energy distribution (SED) fitting procedure described by ⁴. To summarize, this approach used `astroARIADNE` ⁶¹ with the BT-Settl stellar atmosphere models ⁶⁰, assuming the ⁶² solar abundances and the ⁶³ water line lists. This approach fitted for the stellar effective temperature, radius, reddening, surface gravity, metallicity, and distance by comparing the measured broadband magnitudes against pre-computed model grids. Specifically, we performed the fit using the broadband magnitudes from Gaia DR2, APASS, 2MASS, SDSS, and WISE *W1* and *W2*. The resulting best-fit SED is shown in Figure 2. This method has the most constraining power for the star’s effective temperature ($2972 \pm 40\text{ K}$) and radius ($0.42 \pm 0.02 R_\odot$); the surface gravity, metallicity, and reddening are only weakly constrained. We determined the star’s spectral type to be M5.5Ve by visually comparing the HIRES spectra



Extended Data Figure 2: Spectral energy distribution of broadband photometric magnitudes (filled markers) plotted over the best-fit BT-Settl stellar atmosphere model ⁶⁰ and the associated photometric predictions (empty markers). This plot was made from an adaptation of `astroARIADNE` ⁶¹. The photometry extends from the Gaia DR3 blue passband to WISE W3; the W4 passband (22 μm) did not yield a confident detection. This fit yields the star’s temperature and size. The lack of excess infrared flux relative to the photospheric model sets an upper limit on emission from circumstellar dust.

against the photometric standards tabulated by ⁶⁴. This result agrees with the effective temperature found from the SED fitting ⁶⁵. We measured the equivalent width of the $\text{H}\alpha$ line by fitting a range of models to the time-averaged line profile shown in Figure 2, selecting the model that minimized the Bayesian information criterion, and numerically integrating this best fit model. We found a sum of two Gaussians to be the preferred model; our quoted result, $\text{EW}_{\text{H}\alpha} = 7.2 \pm 0.2 \text{ \AA}$, comes from numerically integrating within $|\Delta v/v_{\text{eq}}| < 1$. Integrating over the entire line profile, including the broad wings, would yield $\text{EW}_{\text{H}\alpha} = 10.2 \pm 0.3 \text{ \AA}$. Either value would classify the star as a weak-lined T Tauri ⁶⁶.

Given the effective temperature, stellar radius, and age range (35-150 Myr) derived below, we then estimated the stellar mass by interpolating against the PARSEC v1.2S isochrones ³¹. Specifically, we used the distance metric defined in Equation 8 of ⁴ to select the model mass closest to a given observed temperature, radius, and age. This exercise yielded a mass of $M_{\star} = 0.20 \pm 0.01 M_{\odot}$.

assuming an age of 35 Myr, or a mass of $0.25 \pm 0.01 M_{\odot}$ assuming an age of 150 Myr. These masses imply Keplerian corotation radii $R_{\text{cr}}/R_{\star}=1.75 \pm 0.07$ and $R_{\text{cr}}/R_{\star}=1.89 \pm 0.07$, respectively; this size scale is relevant because it is theoretically expected to set the inner boundary at which corotating material might accumulate (e.g. ^{7,11}). Our final quoted M_{\star} and R_{cr} values adopt the average of these extremes and a quadrature sum of their statistical uncertainties; we caution however that a more precise age would be needed to resolve the systematic uncertainties in these parameters.

Age: No Obvious Association Membership—Previous work ⁴ has found that over 90% of CPVs are associated with known young moving groups based on their positions and kinematics. TIC 141146667 is in the minority. We calculated the probability of TIC 141146667 being part of any nearby known group using BANYAN Σ v1.2 ⁶⁷. That particular model classifies it as a field star at $>99.9\%$ confidence. We also searched the local vicinity of TIC 141146667 for neighbors with similar projected on-sky velocities using `comove` ⁶⁸. This yielded no strong candidates for co-moving stars with projected tangential velocities $\Delta v_{\text{T}} < 5 \text{ km s}^{-1}$ that share its isochronal youth.

Age: Isochrones—The color and absolute magnitude of TIC 141146667 suggest that it is a pre-main sequence M dwarf, similar to all other known CPVs ^{2,4,69}. The star’s proximity ($d=58 \text{ pc}$) and high galactic latitude ($b=+53^{\circ}$) yield negligible interstellar reddening along the line of sight ⁷⁰. Figure 3 shows the location of TIC 141146667 in the color–absolute magnitude diagram (CAMD) relative to young stellar populations including Upper Scorpius (USco), IC 2602, and the Pleiades. To make this diagram, we adopted the USco members in the $\delta \text{ Sco}$ and $\sigma \text{ Sco}$ sub-associations from ⁷¹, and the IC 2602 and Pleiades members from ⁷². We assumed an average V -band extinction $A_V = \{0.12, 0.11, 0.10\} \text{ mag}$ for USco ⁷³, IC 2602 ⁷², and the Pleiades ⁷² respectively, and ages of 8 Myr ⁷¹, 40 Myr ⁷⁴, and 112 Myr ⁷⁵ for each respective cluster. We dereddened the photometry using the extinction coefficients $k_X \equiv A_X/A_0$ tabulated in ⁷⁶, assuming that $A_0 = 3.1E(B - V)$.

Figure 3 shows that TIC 141146667 falls between the USco and Pleiades sequences, and approximately overlaps IC 2602. However, the precision of the implied age is set by the intrinsic scatter of these calibration sequences; the most luminous stars in the Pleiades of the same color have a similar absolute magnitude as TIC 141146667. Previous work ⁶⁹ has also noted that in the Gaia passbands, CPVs tend to be photometrically redder and more luminous than single stars in any given cluster, similar to other rapid rotators. While this effect complicates any attempt at age inference based on the Gaia photometry, it suggests that the Pleiades may be a better comparison population than IC 2602. We take the star’s location in the color–absolute magnitude diagram to suggest age bounds $t_{\text{CAMD}} \sim 30\text{--}150 \text{ Myr}$.

Age: Lithium—The depletion of lithium due to ${}^7\text{Li}(p, \alpha){}^4\text{He}$ burning in the cores of low-mass stars has been studied for over sixty years ^{77–79}. ⁸⁰ provided a recent overview: an abbreviated summary is that sufficiently cool and young M dwarfs show the 6707.8 \AA doublet in absorption, $\gtrsim 10\%$ below their “continua”. Unlike for Sun-like stars, the continuum for M dwarfs is poorly defined due to their molecular absorption. We therefore attempted a lithium measurement by constructing a wavelength-binned and Doppler-corrected TIC 141146667 spectrum, assigning its uncertainties based on the measured scatter across the five hour dataset. We then compared this average spec-

trum against the nearest matching M6 template from ⁶⁴. The data show a small depression near the expected lithium wavelength, potentially consistent with the $\Delta\lambda\approx 3\text{ \AA}$ line broadening. This feature nominally yields $EW_{\text{Li}}=71^{+18}_{-13}\text{ m\AA}$, where the statistical uncertainties are evaluated using a bootstrap resampling technique from the statistical uncertainties in the HIRES spectrum. However, the systematic uncertainties associated with the continuum normalization are likely comparable to the amplitude of this feature; we therefore treat the result of this measurement as a 2σ upper limit: $EW_{\text{Li}} < 107\text{ m\AA}$.

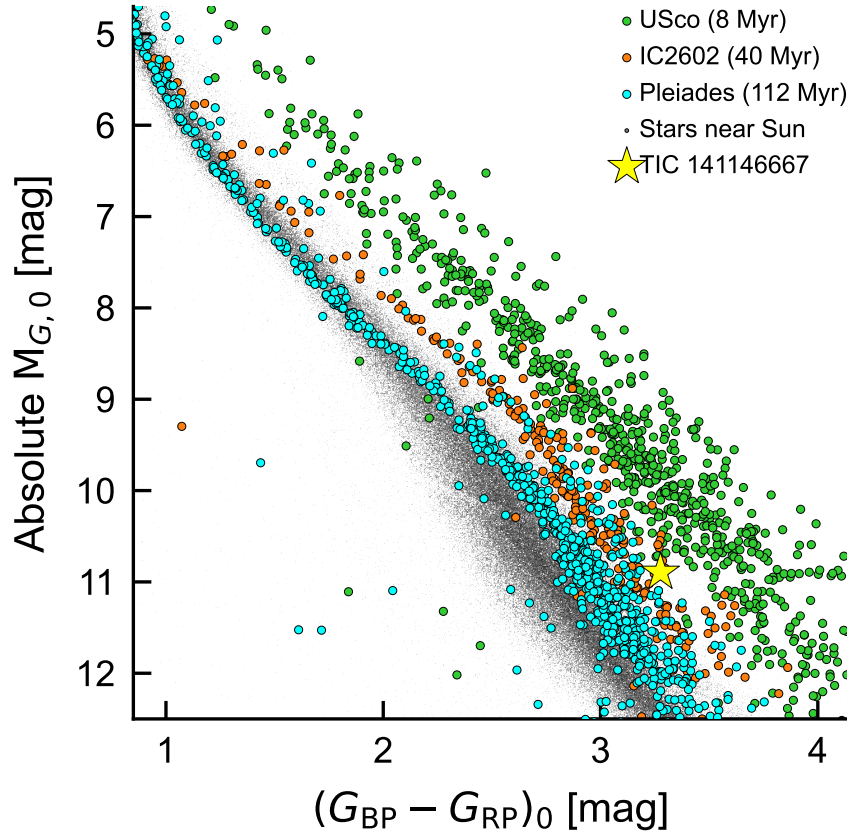
Despite uncertainties in the details, what can be stated with confidence is that lithium is not abundant in the spectrum of TIC 141146667. Figure 4 compares our upper limit against the equivalent width measurements reported by ⁸¹ based on the Gaia-ESO spectroscopic survey; Figure 5 shows the associated raw spectra. If the star were $\lesssim 20\text{ Myr}$ old, at its temperature we would expect to see lithium in abundance ($>400\text{ m\AA}$). Since we do not, we can set an empirical bound on the lithium-derived age of $t_{\text{Li,emp}} \gtrsim 20\text{ Myr}$. The ⁸² lithium isochrones provide a point for theoretical comparison, and suggest that since $M_K \approx 6.67\text{ mag}$, $t_{\text{Li,th}} \gtrsim 35\text{ Myr}$ is the theoretical age at which complete depletion occurs in a star with this luminosity (see e.g. Figure 7 from ⁸⁰).

Age: Summary—The main indicators for the youth of TIC 141146667 are *i*) that it is a complex periodic variable, and *ii*) that it is 1.5 magnitudes brighter (four times more luminous) than main sequence stars of the same color, while showing no indicators for binarity. The first item constitutes evidence for youth since all known CPVs are $\lesssim 200\text{ Myr}$ ⁴. The reference sequences for the Pleiades (112 Myr, ⁷⁵) show a few stars of equal luminosity and the same temperature, suggesting a photometric isochronal age upper limit $\lesssim 150\text{ Myr}$. The weak lithium absorption suggests an age of at least 20 Myr based on an empirical comparison using Gaia-ESO spectra, or at least 35 Myr based on the ⁸² isochrones. These considerations yield our adopted age range of 150 Myr.

Spectroscopic Variability

Figure 5 shows a few regions of interest in the HIRES spectra, which cover 3650-7960 \AA . Higher order Balmer lines including $H\gamma$ and $H\delta$ ($n = 5 \rightarrow 2$ and $n = 6 \rightarrow 2$) do show variability outside the line core. However, this variability is not clearly periodic in the same manner as the emission seen in $H\alpha$. This could be because there are insufficient hydrogen ions in the relevant excited states, or because the spectra have lower precision in these bluer regions. The Ca HK doublet is also detected in emission, while the continuum near it is not. Chromospheric emission from the magnesium triplet is also detected, but these lines are sufficiently blended to be rendered unusable.

Figure 5 provides a novel view on the sudden blue excess that appeared at $\phi \approx 0.2$ in $H\alpha$, $H\gamma$, $H\delta$, and He 5876 \AA . At the same epoch, only $H\alpha$ clearly shows a resolved red excess as well, although $H\gamma$ and $H\delta$ are broadened at this time. Given the sudden rise of this emission in <15 minutes, this sudden blue excess might suggest a more sudden flow, rather than a stable, periodic component. A stellar flare could be a plausible explanation for such a sudden rise. How-



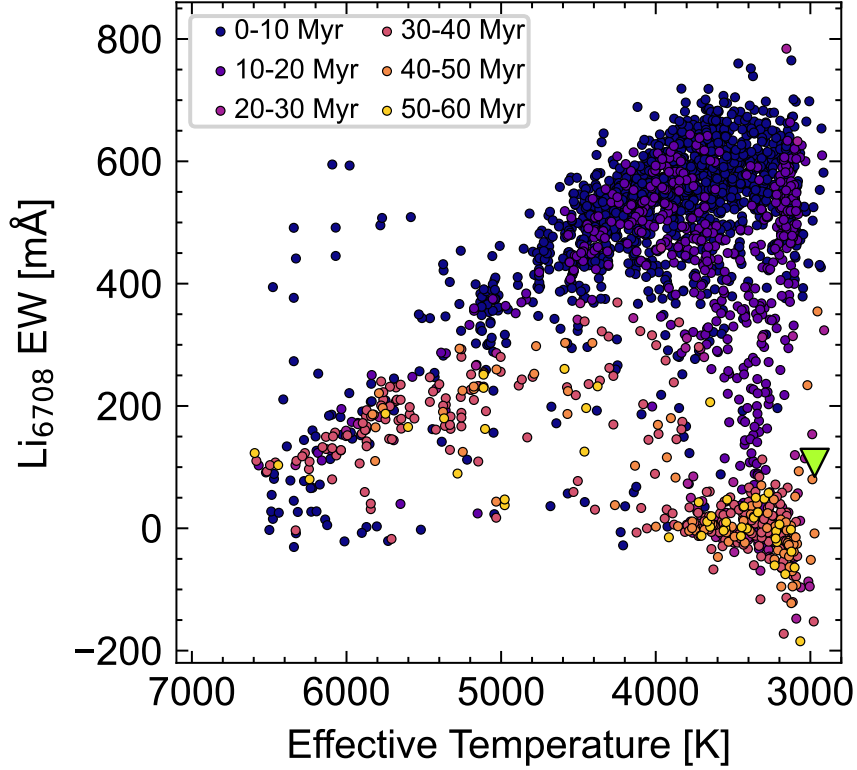
Extended Data Figure 3: Dereddened Gaia DR3 color vs. absolute magnitude diagram of TIC 141146667 and comparison samples. TIC 141146667 is on the pre-main sequence; stars with the same color on the main sequence are ≈ 1.5 magnitudes fainter. The star's location in this diagram suggests an age of 30-150 Myr.

ever this idea seems incompatible with the sinusoidal emission seen from $\phi \approx 0.5$ -1.0, and with the fact that flares often excite iron lines in the blue HIRES orders, which are not observed. More time-series spectroscopy would be needed to provide a definitive clarification for this type of non-periodic variability.

Finally, the Li I 6708 Å doublet, which shows no obvious absorption, as well as the broad K I 7699 Å resonance line are both shown in Figure 5. In the latter, narrow telluric absorption features overlap the blue wing of the line. Neither of these regions shows any notable variability.

Properties of the Plasma and Magnetospheric Environment

The physical conditions inside the plasma clumps, in particular the hydrogen number density, plasma temperature, ionization fraction, and magnetic field strength can be estimated from the available data. We caution that the following estimates are order of magnitude calculations that



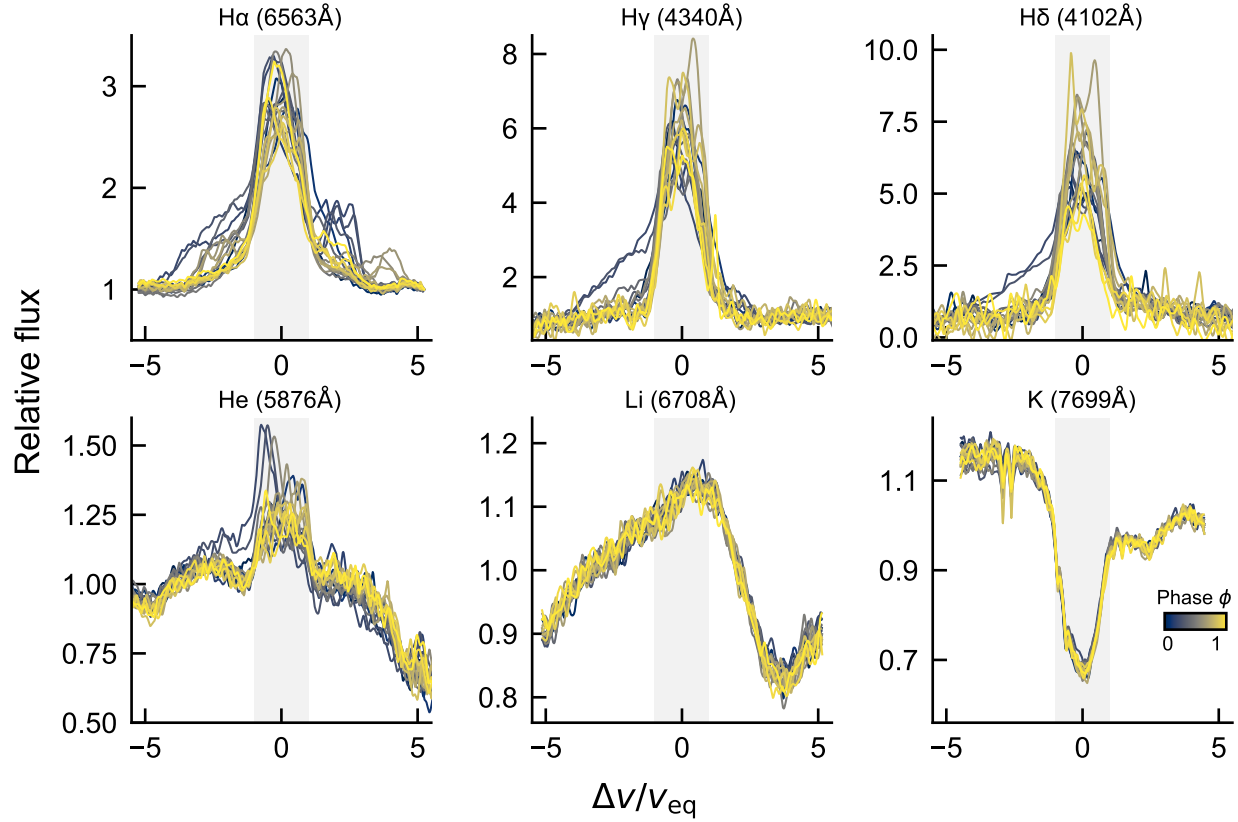
Extended Data Figure 4: An upper limit on photospheric lithium for TIC 141146667 (green triangle) yields a lower bound on the star’s age of $\gtrsim 20$ Myr. Comparison stars are from the Gaia-ESO survey⁸¹; rich clusters in each age bin include NGC 2264 (4.5 Myr), λ Ori (8.7 Myr), γ^2 Vel (16.4 Myr), NGC 2547 (35.0 Myr), IC 2602 and IC 2391 (42.0 Myr), and NGC 2451A (50.0 Myr).

363 assume a simple uniform-density plasma: detailed considerations of radiative transfer are a worthy
 364 topic for future work, but are beyond the scope of this article.

365 Circumstellar $H\alpha$ emission might be sourced either from resonant scattering of stellar $H\alpha$
 366 photons, or from radiative recombination. We neglect scattering because Figures 2 and 5 show
 367 the amplitude of the circumstellar $H\alpha$ emission varying by a factor of ≈ 5 , in a manner uncorre-
 368 lated with any variability in the chromospheric line core. The volume emissivity under case B
 369 recombination can be written

$$j_{H\alpha} = n_e n_p \alpha_{H\alpha}^{\text{eff}} h\nu_{H\alpha}, \quad (1)$$

where n_e and n_p are the electron and proton densities, and $\alpha_{H\alpha}^{\text{eff}}$ is the effective recombination coefficient, defined to include all recombination routes that produce an $H\alpha$ photon. For hydrogen with temperatures between 1,000-10,000 K, $\alpha_{H\alpha}^{\text{eff}}$ is typically on the order of 10^{-12} to $10^{-13} \text{ cm}^3 \text{ s}^{-1}$ ^{83,84}. Neglecting the effects of atoms other than hydrogen, we can assume an ionization fraction x , such that $n_e = n_p = x n_H$, for n_H the hydrogen number density. Let $L_{H\alpha} = j_{H\alpha} V$, for V the volume of the emitting hydrogen. The luminosity of circumstellar hydrogen emission, $L_{H\alpha}$, is an observable: our SED fitting routine yields $L_\star \approx 0.012 L_\odot$, which implies that the stellar $H\alpha$ line



Extended Data Figure 5: Time evolution of select regions in the Keck/HIRES spectra from 17 February 2024. We made this plot by applying a windowed outlier rejection to remove cosmic rays and then smoothing each spectrum with a Gaussian filter. The horizontal axis shows the velocity relative to each line’s rest wavelength, normalized by the stellar equatorial velocity. $H\alpha$ is the only Balmer line to show periodic variability of the form seen in Figure 2. The He 5876 Å line shows a time-dynamic blueshift that differs from the Balmer lines. Li 6708 Å shows no obvious absorption.

radiates at $\approx 1.0 \times 10^{28} \text{ erg s}^{-1}$. The luminosity of the clumps $L_{H\alpha}$ are of order one tenth that of the star. If we approximate the emitting volume as a homogeneous sphere of radius r , we can write

$$n_H = 5 \cdot 10^{11} \text{ cm}^{-3} \left(\frac{0.5}{x} \right) \left(\frac{L_{H\alpha}}{10^{27} \text{ erg s}^{-1}} \frac{10^{-13} \text{ cm}^3 \text{ s}^{-1}}{\alpha_{H\alpha}^{\text{eff}}} \right)^{1/2} \left(\frac{0.04 R_{\odot}}{r} \right)^{3/2}. \quad (2)$$

For a uniform density clump, this suggests a total gas mass of $M_{\text{gas}} \approx 8 \times 10^{16} \text{ g}$. We emphasize that Equation 2 is intended to provide only an order of magnitude estimate for the number density implied by the observed $H\alpha$ emission. In detail, the effective recombination rate and the ionization fraction each vary with density and temperature; a more thorough estimate would iteratively solve the equations of detailed balance and radiative transfer (e.g. ⁶ Figure 8), and potentially also consider departures from local thermodynamic equilibrium.

Finally, a constraint on the magnetic field strength at the site of the clump follows from the requirement that the magnetic pressure exceed the thermal pressure, $B_c^2/8\pi > n_H kT$. Although we do not know the plasma temperature, if it were significantly beyond 1,000-10,000 K, we would either fully ionize the hydrogen, or not ionize enough of it. The field strength at the clump must therefore exceed

$$B_c \gtrsim 3 \text{ G} \left(\frac{n_H}{5 \times 10^{11} \text{ cm}^{-3}} \frac{T}{5000 \text{ K}} \right)^{1/2}. \quad (3)$$

Given that the average surface magnetic field strengths of low-mass stars have been measured to span hundreds to thousands of Gauss⁸⁵⁻⁸⁷, this bound is easily met.

Upper and Lower Bounds on Dust

The material's composition – either pure plasma, or a dusty plasma – is not known. The idea of dust being present seems plausible given observations of chromatic transits in analogous objects^{21,42,43}. However, this scenario is highly constrained. An upper limit on the amount of hot dust follows from the lack of an infrared excess. A lower limit follows if one assumes that most of the broadband optical depth comes from dust absorption and scattering, rather than any radiative processes associated with the plasma.

Regarding the upper limit, Figure 2 shows the SED. While AllWISE⁸⁸ yielded a confident W3 detection (9.8σ), the W4 extraction yielded only a marginal indication (1.7σ) of detectable flux. Similar to other CPVs^{2,4}, the photometric uncertainties from WISE W1 and W2 allow at most a $\lesssim 2\%$ excess at 3-5 μm relative to the stellar photosphere, and a $\lesssim 5\%$ excess at 10 μm (W3). To estimate the implied mass bound, we assume a dust temperature $T_d=1500 \text{ K}$, typical for dust near the star (see¹⁹ for discussion regarding dust sublimation). We then treat emission from the dust and star as Planck functions, and require $L_d < f L_*$, where the factor f is set by the photometric precision of WISE and L_d is the bolometric dust luminosity. Given the reported uncertainties, we numerically find $f < 6 \cdot 10^{-3}$. From the Stefan-Boltzmann law we can then write $A_d < f(T_*/T_d)^4 Q_{\text{em}}^{-1} (4\pi R_*)^2$, for A_d the total emitting surface area of the dust, and Q_{em} an emission efficiency parameter. Converting this constraint to a dust mass requires an assumption regarding the grain properties. We assume a grain density $\rho_d=3 \text{ g cm}^{-3}$ typical for silicate grains, a fixed grain size $a=1 \mu\text{m}$, and no self-absorption. This enables the assumption that $A_d = N\pi a^2$, for N the total number of dust grains. This in turn yields an upper limit on the dust mass of

$$M_{\text{dust}} \lesssim 4 \cdot 10^{17} \text{ g} \left(\frac{f}{6 \cdot 10^{-3}} \right) \left(\frac{T_*}{3000 \text{ K}} \frac{1500 \text{ K}}{T_d} \right)^4 \left(\frac{Q_{\text{em}}}{1} \right)^{-1} \left(\frac{R_*}{0.4 R_\odot} \right)^2 \left(\frac{a}{1 \mu\text{m}} \right) \left(\frac{\rho_d}{3 \text{ g cm}^{-3}} \right). \quad (4)$$

The analogous lower limit follows from requiring the optical depth from absorption and scattering τ to be at least unity. The optical depth can be written $\tau = n\sigma\ell$, where σ is the cross-section, n is the number density, ℓ is the path length. For spherical dust grains in the optical, $\sigma = Q_{\text{ext}}\pi a^2$, where Q_{ext} is the extinction efficiency parameter, tabulated e.g. by⁸⁹ in their Figure 13.⁹⁰ calculated the relevant cloud mass for this problem assuming a spherical dust clump of size

409 r , and they found

$$M_{\text{dust}} \gtrsim 2 \cdot 10^{15} \text{ g} \left(\frac{\tau}{1} \right) \left(\frac{Q_{\text{ext}}}{3} \right)^{-1} \left(\frac{r}{0.1 R_{\star}} \frac{R_{\star}}{0.4 R_{\odot}} \right)^2 \left(\frac{a}{1 \mu\text{m}} \right) \left(\frac{\rho_{\text{d}}}{3 \text{ g cm}^{-3}} \right). \quad (5)$$

410 Three relevant objects for comparison to these limits are solar prominences, planetesimals,
 411 and comets. Prominences of the Sun have gas masses of order 10^{14} g - 10^{16} g ³⁴. A planetesimal
 412 of mass $\approx 10^{15} \text{ g}$ with a bulk density of 1 g cm^{-3} would have a diameter of order one kilometer.
 413 Halley’s comet has a mass of order 10^{17} g ⁹¹, of which $\sim 10^{14} \text{ g}$ is shed per orbit, most of which
 414 inspirals toward the Sun due to Poynting-Robertson drag.

415 These calculations suggest that if dust is responsible for the broadband variability of CPVs,
 416 it would need to be concentrated in clumps with masses in the range of 10^{15} - 10^{17} g . Given
 417 $M_{\text{gas}} \approx 8 \times 10^{16} \text{ g}$ from Section 3, the allowed dust masses imply $M_{\text{gas}}/M_{\text{dust}}$ ranges of 1-100. More
 418 careful measurements of this ratio—in particular enabled by inferring the dust mass through high
 419 precision infrared spectrophotometry—could provide a path for distinguishing the scenario of a
 420 trapped stellar outflow from an accumulation of externally-sourced material.

- 422 1. Rebull, L. M. *et al.* Rotation in the Pleiades with K2. II. Multiperiod Stars. *Astron. J.* **152**,
 423 114 (2016).
- 424 2. Stauffer, J. *et al.* Orbiting Clouds of Material at the Keplerian Co-rotation Radius of Rapidly
 425 Rotating Low-mass WTTs in Upper Sco. *Astron. J.* **153**, 152 (2017).
- 426 3. Rebull, L. M. *et al.* Rotation of Low-mass Stars in Upper Scorpius and ρ Ophiuchus with K2.
 427 *Astron. J.* **155**, 196 (2018).
- 428 4. Bouma, L. G. *et al.* Transient Corotating Clumps around Adolescent Low-mass Stars from
 429 Four Years of TESS. *Astron. J.* **167**, 38 (2024).
- 430 5. Koen, C. Starspot modelling of the TESS light curve of CVSO 30. *Astron. Astrophys.* **647**,
 431 L1 (2021).
- 432 6. Collier Cameron, A. & Robinson, R. D. Fast H-alpha variations on a rapidly rotating cool
 433 main sequence star- I. Circumstellar clouds. *Mon. Not. R. Astron. Soc.* **236**, 57–87 (1989).
- 434 7. Townsend, R. H. D. & Owocki, S. P. A rigidly rotating magnetosphere model for circumstellar
 435 emission from magnetic OB stars. *Mon. Not. R. Astron. Soc.* **357**, 251–264 (2005).
- 436 8. Dunstone, N. J., Collier Cameron, A., Barnes, J. R. & Jardine, M. The coronal structure of
 437 Speedy Mic - II. Prominence masses and off-disc emission. *Mon. Not. R. Astron. Soc.* **373**,
 438 1308–1320 (2006).
- 439 9. Petit, V. *et al.* A magnetic confinement versus rotation classification of massive-star magneto-
 440 spheres. *Mon. Not. R. Astron. Soc.* **429**, 398–422 (2013).

Parameter	Host	Source
Identifiers		
TIC	141146667	TESS
Gaia	860453786736413568	Gaia DR3
Astrometry & Radial Velocity		
α_{2000}	11:05:15.09	Gaia DR3
δ_{2000}	+59 15 05.57	Gaia DR3
μ_{α} (mas yr ⁻¹)	-73.933 ± 0.022	Gaia DR3
μ_{δ} (mas yr ⁻¹)	32.262 ± 0.024	Gaia DR3
π (mas)	17.324 ± 0.025	Gaia DR3
RUWE	1.23	Gaia DR3
RV (km s ⁻¹)	0.61 ± 1.47	HIRES
Photometry		
<i>TESS</i> (mag)	13.283 ± 0.010	TIC8
<i>G</i> (mag)	14.701 ± 0.002	Gaia DR3
<i>G</i> _{BP} (mag)	16.664 ± 0.008	Gaia DR3
<i>G</i> _{RP} (mag)	13.398 ± 0.006	Gaia DR3
<i>G</i> _{BP} - <i>G</i> _{RP} (mag)	3.276 ± 0.010	Gaia DR3
<i>J</i> (mag)	11.401 ± 0.022	2MASS
<i>H</i> (mag)	10.793 ± 0.021	2MASS
<i>K_s</i> (mag)	10.473 ± 0.016	2MASS
<i>W1</i> (mag)	10.276 ± 0.023	ALLWISE
<i>W2</i> (mag)	10.070 ± 0.020	ALLWISE
<i>W3</i> (mag)	9.838 ± 0.045	ALLWISE
Physical Properties		
<i>T_{eff}</i> (K)	2972 ± 40	⁴ SED fit
<i>R</i> _★ (<i>R</i> _☉)	0.42 ± 0.02	⁴ SED fit
<i>L</i> _★ (<i>L</i> _☉)	0.0126 ± 0.0012	⁴ SED fit
<i>P</i> _{rot} (hours)	3.930 ± 0.001	TESS
<i>v</i> _{eq} (km s ⁻¹)	130±4	Derived
<i>v</i> _{eq} sin <i>i</i> _★ (km s ⁻¹)	138 ± 8	HIRES
<i>i</i> _★ (°)	>63	Derived
<i>A_V</i> (mag)	0	⁷⁰
<i>M</i> _★ (<i>M</i> _☉)	0.22 ± 0.02	PARSEC ³¹
EW _{Li} (mÅ)	<107	HIRES (2σ)
<i>t</i> _{CAMD} (Myr)	30-150	Gaia DR3
<i>t</i> _{Li,emp} (Myr)	>20	HIRES, ⁸¹
<i>t</i> _{Li,th} (Myr)	>35	HIRES, ⁸²
<i>t</i> _{adopted} (Myr)	35-150	—

Extended Data Table 1: Properties of TIC 141146667. References: Gaia DR3 ³², TESS ²⁸, TIC8 ⁹², 2MASS ⁹³, ALLWISE ⁸⁸.

Time [BJD _{TDB}]	RV (km s ⁻¹)	σ_{RV} (km s ⁻¹)
2460357.954919	2.73	5.86
2460357.965845	-4.40	2.37
2460357.976770	-0.19	2.64
2460357.987698	3.84	2.87
2460357.998619	7.53	7.53
2460358.009538	-1.98	1.44
2460358.020462	1.02	1.21
2460358.031383	0.64	7.03
2460358.042306	-2.91	2.71
2460358.053228	8.93	6.75
2460358.064154	5.95	8.84
2460358.075075	-2.25	3.06
2460358.085996	1.84	1.34
2460358.096918	2.41	8.24
2460358.107839	-7.04	3.94
2460358.118760	-2.24	3.07
2460358.129683	-2.83	7.55
2460358.140606	-0.59	2.26
2460358.151527	1.84	2.91
2460358.162448	4.54	3.95
2460358.173368	6.21	12.14

Extended Data Table 2: TIC 141146667 radial velocities relative to the systemic velocity.

10. Waugh, R. F. P. & Jardine, M. M. Magnetic confinement of dense plasma inside (and outside) stellar coronae. *Mon. Not. R. Astron. Soc.* **514**, 5465–5477 (2022).
11. Daley-Yates, S. & Jardine, M. M. Simulating stellar coronal rain and slingshot prominences. *Mon. Not. R. Astron. Soc.* **534**, 621–633 (2024).
12. National Academies of Sciences, E. & Medicine. *Pathways to Discovery in Astronomy and Astrophysics for the 2020s* (The National Academies Press, Washington, DC, 2023). URL <https://nap.nationalacademies.org/catalog/26141/pathways-to-discovery-in-astronomy-and-astrophysics-for-the-2020s>.
13. Redfield, S. *et al.* Report of the Working Group on Strategic Exoplanet Initiatives with HST and JWST. *arXiv e-prints* arXiv:2404.02932 (2024).
14. TRAPPIST-1 JWST Community Initiative *et al.* A roadmap for the atmospheric characterization of terrestrial exoplanets with JWST. *Nature Astronomy* **8**, 810–818 (2024).
15. Dressing, C. D. & Charbonneau, D. The Occurrence of Potentially Habitable Planets Orbiting M Dwarfs Estimated from the Full Kepler Dataset and an Empirical Measurement of the Detection Sensitivity. *Astrophys. J.* **807**, 45 (2015).
16. Ribas, Á., Bouy, H. & Merín, B. Protoplanetary disk lifetimes vs. stellar mass and possible implications for giant planet populations. *Astron. Astrophys.* **576**, A52 (2015).
17. France, K. *et al.* The Ultraviolet Radiation Environment around M dwarf Exoplanet Host Stars. *Astrophys. J.* **763**, 149 (2013).
18. Günther, M. N. *et al.* Stellar Flares from the First TESS Data Release: Exploring a New Sample of M Dwarfs. *Astron. J.* **159**, 60 (2020).
19. Zhan, Z. *et al.* Complex Rotational Modulation of Rapidly Rotating M Stars Observed with TESS. *Astrophys. J.* **876**, 127 (2019).
20. Rebull, L. M. *et al.* Rotation of Low-mass Stars in Taurus with K2. *Astron. J.* **159**, 273 (2020).
21. Günther, M. N. *et al.* Complex Modulation of Rapidly Rotating Young M Dwarfs: Adding Pieces to the Puzzle. *Astron. J.* **163**, 144 (2022).
22. Collier Cameron, A. & Woods, J. A. Prominence activity in G dwarfs of the alpha Persei cluster. *Mon. Not. R. Astron. Soc.* **258**, 360–370 (1992).
23. Barnes, J. R., Collier Cameron, A., James, D. J. & Donati, J. F. Doppler images from dual-site observations of southern rapidly rotating stars - I. Differential rotation on PZ Tel. *Mon. Not. R. Astron. Soc.* **314**, 162–174 (2000).
24. Donati, J. F. *et al.* Surface differential rotation and prominences of the Lupus post T Tauri star RX J1508.6-4423. *Mon. Not. R. Astron. Soc.* **316**, 699–715 (2000).

25. Skelly, M. B. *et al.* Doppler images and chromospheric variability of TWA 6. *Mon. Not. R. Astron. Soc.* **385**, 708–718 (2008).
26. Leitzinger, M. *et al.* Indications of stellar prominence oscillations on fast rotating stars: the cases of HK Aqr and PZ Tel. *Mon. Not. R. Astron. Soc.* **463**, 965–979 (2016).
27. Cang, T. Q., Petit, P., Donati, J. F. & Folsom, C. P. Short-term variations of surface magnetism and prominences of the young Sun-like star V530 Per. *Astron. Astrophys.* **654**, A42 (2021).
28. Ricker, G. R. *et al.* Transiting Exoplanet Survey Satellite (TESS). *Journal of Astronomical Telescopes, Instruments, and Systems* **1**, 014003 (2015).
29. Vogt, S. S. *et al.* *SPIE Conference Series*, vol. 2198 (1994).
30. Townsend, R. H. D. Exploring the photometric signatures of magnetospheres around helium-strong stars. *Mon. Not. R. Astron. Soc.* **389**, 559–566 (2008).
31. Chen, Y. *et al.* Improving PARSEC models for very low mass stars. *Mon. Not. R. Astron. Soc.* **444**, 2525–2543 (2014).
32. Gaia Collaboration *et al.* Gaia Data Release 3. Summary of the content and survey properties. *Astron. Astrophys.* **674**, A1 (2023).
33. Cang, T. Q. *et al.* Magnetic field and prominences of the young, solar-like, ultra-rapid rotator V530 Persei. *Astron. Astrophys.* **643**, A39 (2020).
34. Vial, J.-C. & Engvold, O. *Solar Prominences*, vol. 415 of *Astrophysics and Space Science Library* (2015).
35. Bagenal, F. & Sullivan, J. D. Direct plasma measurements in the Io torus and inner magnetosphere of Jupiter. *J. Geophys. Res.* **86**, 8447–8466 (1981).
36. Berry, I. D., Owocki, S. P., Shultz, M. E. & ud-Doula, A. Electron scattering emission in the light curves of stars with centrifugal magnetospheres. *Mon. Not. R. Astron. Soc.* **511**, 4815–4825 (2022).
37. Mikulášek, Z. *et al.* What’s New with Landstreet’s Star HD 37776 (V901 Ori)? In Wade, G., Alecian, E., Bohlender, D. & Sigut, A. (eds.) *Stellar Magnetism: A Workshop in Honour of the Career and Contributions of John D. Landstreet*, vol. 11, 46–53 (2020). 1912.04121.
38. Kochukhov, O., Lundin, A., Romanyuk, I. & Kudryavtsev, D. The Extraordinary Complex Magnetic Field of the Helium-strong Star HD 37776. *Astrophys. J.* **726**, 24 (2011).
39. Shultz, M. E. *et al.* The magnetic early B-type stars I: magnetometry and rotation. *Mon. Not. R. Astron. Soc.* **475**, 5144–5178 (2018).
40. Johns-Krull, C. M. *et al.* H α Variability in PTFO8-8695 and the Possible Direct Detection of Emission from a 2 Million Year Old Evaporating Hot Jupiter. *Astrophys. J.* **830**, 15 (2016).

41. Bouma, L. G. *et al.* PTFO 8-8695: Two Stars, Two Signals, No Planet. *Astron. J.* **160**, 86 (2020).
42. Tanimoto, Y. *et al.* Evidence for planetary hypothesis for PTFO 8-8695 b with five-year optical/infrared monitoring observations. *PASJ* **72**, 23 (2020).
43. Koen, C. Multifilter observations of the complex periodic variations in eight pre-main sequence stars. *Mon. Not. R. Astron. Soc.* **518**, 2921–2937 (2023).
44. Rackham, B. V., Apai, D. & Giampapa, M. S. The Transit Light Source Effect: False Spectral Features and Incorrect Densities for M-dwarf Transiting Planets. *Astrophys. J.* **853**, 122 (2018).
45. Reach, W. T., Lisse, C., von Hippel, T. & Mullally, F. The Dust Cloud around the White Dwarf G 29-38. II. Spectrum from 5 to 40 μm and Mid-Infrared Photometric Variability. *Astrophys. J.* **693**, 697–712 (2009).
46. Marigo, P. *et al.* Evolution of asymptotic giant branch stars. II. Optical to far-infrared isochrones with improved TP-AGB models. *Astron. Astrophys.* **482**, 883–905 (2008).
47. Krtićka, J., Mikulášek, Z., Kurfürst, P. & Oksala, M. E. Photometric signatures of corotating magnetospheres of hot stars governed by higher-order magnetic multipoles. *Astron. Astrophys.* **659**, A37 (2022).
48. Brown, B. P., Oishi, J. S., Vasil, G. M., Lecoanet, D. & Burns, K. J. Single-hemisphere Dynamos in M-dwarf Stars. *Astrophys. J.* **902**, L3 (2020).
49. Kaur, S. *et al.* Hints of auroral and magnetospheric polarized radio emission from the scallop-shell star 2MASS J05082729–2101444. *Astron. Astrophys.* **691**, L17 (2024).
50. Callingham, J. R. *et al.* The population of M dwarfs observed at low radio frequencies. *Nature Astronomy* **5**, 1233–1239 (2021).
51. Howard, A. W. *et al.* The California Planet Survey. I. Four New Giant Exoplanets. *Astrophys. J.* **721**, 1467–1481 (2010).
52. Husser, T. O. *et al.* A new extensive library of PHOENIX stellar atmospheres and synthetic spectra. *Astron. Astrophys.* **553**, A6 (2013).
53. Chubak, C. *et al.* Precise Radial Velocities of 2046 Nearby FGKM Stars and 131 Standards. *arXiv e-prints* arXiv:1207.6212 (2012).
54. Kanodia, S. & Wright, J. Python Leap Second Management and Implementation of Precise Barycentric Correction (barycorrpy). *Research Notes of the American Astronomical Society* **2**, 4 (2018).
55. Gray, D. F. *The Observation and Analysis of Stellar Photospheres* (2008).

56. Stellingwerf, R. F. Period determination using phase dispersion minimization. *Astrophys. J.* **224**, 953–960 (1978).
57. Bhatti, W. *et al.* waqasbhatti/astrobase: astrobase v0.5.3. Zenodo (2021).
58. Tokovinin, A. & Briceño, C. Yes, Multi-periodic Dwarfs in Upper Scorpius Are Binaries. *Astron. J.* **156**, 138 (2018).
59. Winters, J. G. *et al.* The Solar Neighborhood. XLV. The Stellar Multiplicity Rate of M Dwarfs Within 25 pc. *Astron. J.* **157**, 216 (2019).
60. Allard, F., Homeier, D. & Freytag, B. Models of very-low-mass stars, brown dwarfs and exoplanets. *Philosophical Transactions of the Royal Society A: Mathematical, Physical and Engineering Sciences* **370**, 2765–2777 (2012).
61. Vines, J. I. & Jenkins, J. S. ARIADNE: measuring accurate and precise stellar parameters through SED fitting. *Mon. Not. R. Astron. Soc.* **513**, 2719–2731 (2022).
62. Asplund, M., Grevesse, N., Sauval, A. J. & Scott, P. The Chemical Composition of the Sun. *ARA&A* **47**, 481–522 (2009).
63. Barber, R. J., Tennyson, J., Harris, G. J. & Tolchenov, R. N. A high-accuracy computed water line list. *Mon. Not. R. Astron. Soc.* **368**, 1087–1094 (2006).
64. Bochanski, J. J., West, A. A., Hawley, S. L. & Covey, K. R. Low-Mass Dwarf Template Spectra from the Sloan Digital Sky Survey. *Astron. J.* **133**, 531–544 (2007).
65. Pecaution, M. J. & Mamajek, E. E. Intrinsic Colors, Temperatures, and Bolometric Corrections of Pre-main-sequence Stars. *Astrophys. J. Suppl.* **208**, 9 (2013).
66. Briceño, C. *et al.* The CIDA Variability Survey of Orion OB1. II. Demographics of the Young, Low-mass Stellar Populations. *Astron. J.* **157**, 85 (2019).
67. Gagné, J. *et al.* BANYAN. XI. The BANYAN Σ Multivariate Bayesian Algorithm to Identify Members of Young Associations with 150 pc. *Astrophys. J.* **856**, 23 (2018).
68. Tofflemire, B. M. *et al.* TESS Hunt for Young and Maturing Exoplanets (THYME). V. A Sub-Neptune Transiting a Young Star in a Newly Discovered 250 Myr Association. *Astron. J.* **161**, 171 (2021).
69. Stauffer, J. *et al.* Even More Rapidly Rotating Pre-main-sequence M Dwarfs with Highly Structured Light Curves: An Initial Survey in the Lower Centaurus-Crux and Upper Centaurus-Lupus Associations. *Astron. J.* **161**, 60 (2021).
70. Green, G. M., Schlafly, E., Zucker, C., Speagle, J. S. & Finkbeiner, D. A 3D Dust Map Based on Gaia, Pan-STARRS 1, and 2MASS. *Astrophys. J.* **887**, 93 (2019).

71. Ratzenböck, S. *et al.* Significance mode analysis (SigMA) for hierarchical structures. An application to the Sco-Cen OB association. *Astron. Astrophys.* **677**, A59 (2023).
72. Hunt, E. L. & Reffert, S. Improving the open cluster census. III. Using cluster masses, radii, and dynamics to create a cleaned open cluster catalogue. *Astron. Astrophys.* **686**, A42 (2024).
73. Pecaution, M. J. & Mamajek, E. E. The star formation history and accretion-disc fraction among the K-type members of the Scorpius-Centaurus OB association. *Mon. Not. R. Astron. Soc.* **461**, 794–815 (2016).
74. Randich, S. *et al.* The Gaia-ESO Survey: open clusters in Gaia-DR1 . A way forward to stellar age calibration. *Astron. Astrophys.* **612**, A99 (2018).
75. Dahm, S. E. Reexamining the Lithium Depletion Boundary in the Pleiades and the Inferred Age of the Cluster. *Astrophys. J.* **813**, 108 (2015). URL <https://ui.adsabs.harvard.edu/abs/2015ApJ...813..108D>.
76. Gaia Collaboration *et al.* Gaia Data Release 2. Summary of the contents and survey properties. *Astron. Astrophys.* **616**, A1 (2018).
77. Hayashi, C. & Nakano, T. Evolution of Stars of Small Masses in the Pre-Main-Sequence Stages. *Progress of Theoretical Physics* **30**, 460–474 (1963).
78. Bildsten, L., Brown, E. F., Matzner, C. D. & Ushomirsky, G. Lithium Depletion in Fully Convective Pre-Main-Sequence Stars. *Astrophys. J.* **482**, 442–447 (1997).
79. Burke, C. J., Pinsonneault, M. H. & Sills, A. Theoretical Examination of the Lithium Depletion Boundary. *Astrophys. J.* **604**, 272–283 (2004).
80. Wood, M. L. *et al.* TESS Hunt for Young and Maturing Exoplanets (THYME). IX. A 27 Myr Extended Population of Lower Centaurus Crux with a Transiting Two-planet System. *Astron. J.* **165**, 85 (2023).
81. Jeffries, R. D. *et al.* The Gaia-ESO Survey: empirical estimates of stellar ages from lithium equivalent widths (EAGLES). *Mon. Not. R. Astron. Soc.* **523**, 802–824 (2023).
82. Feiden, G. A. Magnetic inhibition of convection and the fundamental properties of low-mass stars. III. A consistent 10 Myr age for the Upper Scorpius OB association. *Astron. Astrophys.* **593**, A99 (2016).
83. Hummer, D. G. & Storey, P. J. Recombination-line intensities for hydrogenic ions - I. Case B calculations for H I and He II. *Mon. Not. R. Astron. Soc.* **224**, 801–820 (1987).
84. Draine, B. T. *Physics of the Interstellar and Intergalactic Medium* (2011).
85. Donati, J. F. & Landstreet, J. D. Magnetic Fields of Nondegenerate Stars. *ARA&A* **47**, 333–370 (2009).

86. Kochukhov, O. Magnetic fields of M dwarfs. *A&A Rev.* **29**, 1 (2021).
87. Reiners, A. *et al.* Magnetism, rotation, and nonthermal emission in cool stars. Average magnetic field measurements in 292 M dwarfs. *Astron. Astrophys.* **662**, A41 (2022).
88. Cutri, R. M. *et al.* VizieR Online Data Catalog: AllWISE Data Release (Cutri+ 2013). *VizieR Online Data Catalog* II/328 (2021).
89. Croll, B. *et al.* Multiwavelength Observations of the Candidate Disintegrating Sub-Mercury KIC 12557548b. *Astrophys. J.* **786**, 100 (2014).
90. Sanderson, H., Jardine, M., Collier Cameron, A., Morin, J. & Donati, J. F. Can scallop-shell stars trap dust in their magnetic fields? *Mon. Not. R. Astron. Soc.* **518**, 4734–4745 (2023).
91. Rickman, H. The nucleus of comet Halley: Surface structure, mean density, gas and dust production. *Advances in Space Research* **9**, 59–71 (1989).
92. Stassun, K. G. *et al.* The Revised TESS Input Catalog and Candidate Target List. *Astron. J.* **158**, 138 (2019).
93. Skrutskie, M. F. *et al.* The Two Micron All Sky Survey (2MASS). *Astron. J.* **131**, 1163–1183 (2006).

Acknowledgments LGB is grateful to M. Jardine, A. Weinberger, B. Tofflemire, and J. Spake for insightful conversations, and to A. Howard and H. Isaacson for their assistance reducing the HIRES spectra. This work was supported by the Carnegie Fellowship and by the Heising-Simons 51 Pegasi b Fellowship. Funding for the TESS mission is provided by NASA’s Science Mission directorate. The TESS mission is a product of millions of hours of work by thousands of people; we thank the TESS team for their efforts to make the mission a continued success. The HIRES data were obtained at the Keck Observatory, which exists through a similar scale of community effort. We recognize the importance that the summit of Maunakea has always had within the indigenous Hawaiian community, and we are deeply grateful for the opportunity to conduct observations from this mountain.

Author Contributions LGB is responsible for all aspects of this work, including conceptualization, data analysis, interpretation, manuscript preparation, and revision.

Data Availability The TESS two-minute cadence data used in this work are publicly available from the Mikulski Archive for Space Telescopes (MAST; <https://mast.stsci.edu>). The Keck/HIRES spectra analyzed here are accessible via the Keck Observatory Archive (KOA; <https://koa.ipac.caltech.edu>).

Competing Interests The author declares no competing financial interests.

Correspondence Correspondence and requests for materials should be addressed to Luke Bouma, at either lbouma@carnegiescience.edu or bouma.luke@gmail.com.

638 **Code availability** We provide access to a GitHub repository including all code created for the analysis of
639 this project that is not already publicly available.